Geodesy and Geodynamics 9 (2018) 252–261

Contents lists available at ScienceDirect

Geodesy and Geodynamics

journal homepage: http://www.keaipublishing.com/en/journals/geodesy-and-geodynamics/

An image segmentation based algorithm for imaging of slow slip earthquakes☆

Mohammad Hazrati Kashi [a, *], Noorbakhsh Mirzaei [a], Behzad Moshiri [b]

[a] Institute of Geophysics, University of Tehran, Tehran, Iran
[b] School of Electrical and Computer Engineering, Control and Intelligent Processing Centre of Excellence, University of Tehran, Tehran, Iran

ARTICLE INFO

Article history:
Received 21 December 2016
Received in revised form
16 March 2018
Accepted 4 April 2018
Available online 14 April 2018

Keywords:
Slow-slip earthquakes
Kalman filter
Over smoothing
Image segmentation
Unscented transform

ABSTRACT

Laboratory experiments next to a variety of observations, especially in subduction zones, have explored the existence of a premonitory stable slow slip growth phase preceding large earthquakes. These phenomena play an important role in the earthquake cycle and thus precise imaging and monitoring of these events are of great significance. In the literature, ENIF (extended network inversion filter) has been proposed as a rigorous algorithm capable of isolating signal from different types of noise and thereby provides us with deep insight into spatio-temporal evolution of slow slip events. Despite its considerable advantages, ENIF still suffers from some limitations. ENIF applies Tikhonov method of regularization with a quadratic form of cost function. While anomalous slip regions have clear contrast with the background slip in reality, Tikhonov regularization tends to over smooth (globally smooth) the slipping portion on the estimated images. In order to avoid over smoothing phenomenon, we have incorporated into ENIF an image segmentation step which tries to preserve edges of slow-slip event. As a second limitation, due to the nonlinearity imposed by such constraint as non-negativity of slip rate, uncertainty propagation through model is not simple. As the core of ENIF, EKF (extended Kalman filter), performs uncertainty propagation by linearization of nonlinear model using Jacobian and Hessian matrices. As an alternative for EKF, we have also investigated the application of UKF (unscented Kalman filter) which uses UT (unscented transform) for uncertainty propagation. Finally, we tested our proposed algorithm using a low signal to noise ratio synthetic data set. The results show a significant improvement in the performance of ENIF when the segmentation step is incorporated into the algorithm.

© 2018 Institute of Seismology, China Earthquake Administration, etc. Production and hosting by Elsevier B.V. on behalf of KeAi Communications Co., Ltd. This is an open access article under the CC BY-NC-ND license (http://creativecommons.org/licenses/by-nc-nd/4.0/).

1. Introduction

Laboratory experiments next to a variety of observations, especially in subduction zones, have explored the existence of a premonitory stable slow slip growth phase preceding large earthquakes [1–3]. These phenomena play an important role in the earthquake cycle such as great impact on the moment budget of the fault, stress transfer and redistribution in the crust, impact on nucleation and triggering processes, and triggering earthquake swarms [4–6]. They are also considered as a potential earthquake precursor especially in subduction zones. For example, in the 2011 Mw9.0 Tohoku-Oki megathrust earthquake, a slow slip event was detected before the main shock [3]. As a result, precise imaging and monitoring of these events using crustal deformation data sets are of great significance in tectonic and seismotectonic studies.

Besides developing highly dense, continuous and large scale geodetic arrays such as GEONET (GPS Earth Observatory Network) and the PANGA (Pacific Northwest Geodetic Array), the need for an efficient processing technique for slow slip studies is crucial. In this regard, we are facing with some challenges. First, because our signal of interest, which is related to the slip on the fault, has been

☆ **Session:** Geodynamics and the earthquake cycle (**Conveners:** Kosuke Heki, Janusz Bogusz).

* Corresponding author.
E-mail addresses: m.hazrati@ut.ac.ir (M.H. Kashi), nmirzaii@ut.ac.ir (N. Mirzaei), moshiri@ut.ac.ir (B. Moshiri).

Peer review under responsibility of Institute of Seismology, China Earthquake Administration.

Production and Hosting by Elsevier on behalf of KeAi

https://doi.org/10.1016/j.geog.2018.04.001

1674-9847/© 2018 Institute of Seismology, China Earthquake Administration, etc. Production and hosting by Elsevier B.V. on behalf of KeAi Communications Co., Ltd. This is an open access article under the CC BY-NC-ND license (http://creativecommons.org/licenses/by-nc-nd/4.0/).

contaminated with different types of noise sources like local benchmark motion, measuring device errors, etc., the imaging problem is not straightforward and is thus challenging [7]. Furthermore, we don't have knowledge about functional form of spatio-temporal evolution of these events which means that we are facing with a non-parametric modeling problem [8].

In the literature, McGuire and Segall [9] have developed ENIF (extended network inversion filter) which is a rigorous algorithm capable of isolating signal from different types of noise. This technique provides us with a powerful tool for studying spatio-temporal evolution of slow slip events. To date, considerable advantages have been enumerated for applying this filter. Since EKF (extended Kalman filter) forms the core of ENIF and EKF is in turn a framework for data fusion, it is possible to combine different types of surface deformation data sets (e.g. GPS, GNSS InSAR, UpSAR) via ENIF [10]. Furthermore, as a variant of Sequential Bayesian Filter, EKF is also an effective tool for stochastic estimation of slip, slip rate and more importantly their associated uncertainties [11]. Finally, being a time domain filter, ENIF yields an automatic method for detecting and monitoring of slow slip events.

Despite its considerable advantages, ENIF still suffers from some limitations. ENIF applies Tikhonov method of regularization with Laplacian operator in the form of quadratic cost function. While anomalous slip regions have clear contrast with the background slip in reality, Tikhonov regularization tends to over smooth (globally smooth) the slipping portion on the estimated images. This situation results in images with blurred edges of anomalous regions. Over smoothing is a common challenge among a variety of imaging problems, particularly in the field of medical imaging of dSPECT (dynamic single-photon emission computed tomography). In this study, we are going to reapply some effective measures taken by dSPECT imaging experts to our case of slow slip imaging problem [12,13]. In this regard, we have incorporated into ENIF an image segmentation step in combination with some mathematical morphology operations aiming to detect slipping portion on the fault. In the next step, by some changes in the ENIF formulation, we enforce this filter to focus smoothing just onto the slipping portion of the fault.

As the second limitation, with regard to the nonlinearity imposed by non-negativity constraint of slip rate, uncertainty propagation through nonlinear model is not simple. The EKF performs uncertainty propagation by linearization of nonlinear models in the form of Jacobian and Hessian matrices. Nevertheless, linearization is reliable only under specific circumstances. For example, EKF yields reliable results only when linearization approximates error propagation. Furthermore, Jacobian and Hessian matrices do not exist in all problems or in the cases of existence, their calculation are difficult and apt to human errors [14,15]. Accordingly, as an alternative for EKF, we have also investigated the application of UKF (unscented Kalman filter) which uses UT (unscented transform) for uncertainty propagation.

In the following sections, we will first describe the standard ENIF formulation along with a detailed description of changes in the ENIF. Then a brief description of UT is presented. Finally, using a low signal to noise ratio synthetic data set, the performance of our proposed algorithm will be compared with the standard ENIF.

2. Methods

McGuire and Segall [9] developed ENIF which is a recursive filter for estimation of spatio-temporal changes in slip and slip rate on the faults and subduction zones. In this context, surface displacements recorded by GPS stations as a function of time t, are modeled as the following expression

$$X(t) = \sum_k H\left(t - t_{\mathrm{eq}(k)}\right) X^{\cos(k)} + \int_A s_p(\xi, t - t_0) G^r_{pq}(x, \xi) n_q(\xi) \mathrm{d}A(\xi) + Ff(t) + L(x, t - t_0) + \epsilon \tag{1}$$

where the first term in the right hand side indicates coseismic offsets $X^{\cos(k)}$ resulting from earthquakes at different times t_{eq}, and $H(t)$ is the Heavyside function. Since we are going to address a pure aseismic slip in this study, this term has been excluded from our calculations. The second term represents deformation due to slow slip events with an initiation time of t_0. In this term, $G^r_{pq}(x, \xi)$ is the Green's function relating site displacements to the slip on the fault. The Green's functions applied in this study is derived from analytical expression for uniform half-spaces, although there are also some sophisticated Green's function for heterogeneous and layered medium. $n_q(\xi)$ is the unit normal to the faults surface $A(\xi)$ and the summation is performed on repeated indexes ($p,q,r = 1,2,3$). Finally, the last three terms indicates reference frame errors $Ff(t)$, random benchmark motions $L(x, t - t_0)$, and measurement errors ϵ, respectively. In this study, for the sake of simplicity we have also omitted the reference frame term from calculations.

EKF, which forms the core of ENIF, uses state space modeling to estimate state vector containing all required quantities for imaging problem. The state vector contains two sets of states; the first is concerned with slip and slip rate on each subfault, $(S^i_k, \dot{S}^i_k, \lambda^i_k)$ and the second set models random benchmark motion in each GPS station (β^j_k). The quantities S and $\dot{S}$ indicate slip and slip rate, and λ is a dummy variable to guarantee the non-negativity of slip rate. The superscripts i and j respectively represent the indices of subfault and GPS stations and the subscript k indicates the time step. To estimate state vector in each time step k, EKF uses two models, measurement and process models. The measurement model relates the state vector to the observed data and the process model relates the state vector in the previous time step k-1, to the current time step k. The algorithm begins with an initial estimate for state vector as well as its associated covariance matrix at the first time step. Then, the state vector at the next time step is predicted using process model and again this predicted state vector is updated (corrected) using measurement model and corresponding observed data. This procedure continues iteratively until all the observed data in the time series are processed [16]. Fig. 1 illustrates a complete picture on how EKF performs as the core of ENIF.

The data vector at each time step k, contains three different types of values $\boldsymbol{z}_k = [z^{\mathrm{GPS}}_k, z^{\nabla}_k, z^{+}_k]$. These data types includes GPS observations z^{GPS}_k, pseudo-data regarding spatial smoothing z^{∇}_k, and pseudo-data responsible for non-negativity of slip rates z^{+}_k. The measurement model is stated as the following expressions

$$z^{\mathrm{GPS}}_k = G_{ij} S^j_k + \beta^i_k + \epsilon^i_k, \qquad \epsilon_k \sim N\left(0, \sigma^2 \Sigma^{\mathrm{GPS}}_k\right) \tag{2}$$

$$z^{\nabla}_k = 0 = \nabla^2 \dot{S}_k + \epsilon_k, \qquad \epsilon_k \sim N\left(0, \gamma^2 I\right) \tag{3}$$

$$z^{+}_k = 0 = \dot{S}^i_k - \lambda^{i^2}_k + \epsilon_k, \qquad \epsilon_k \sim N\left(0, \rho^2 I\right) \tag{4}$$

In addition, the covariance matrix associated with data vector is represented as

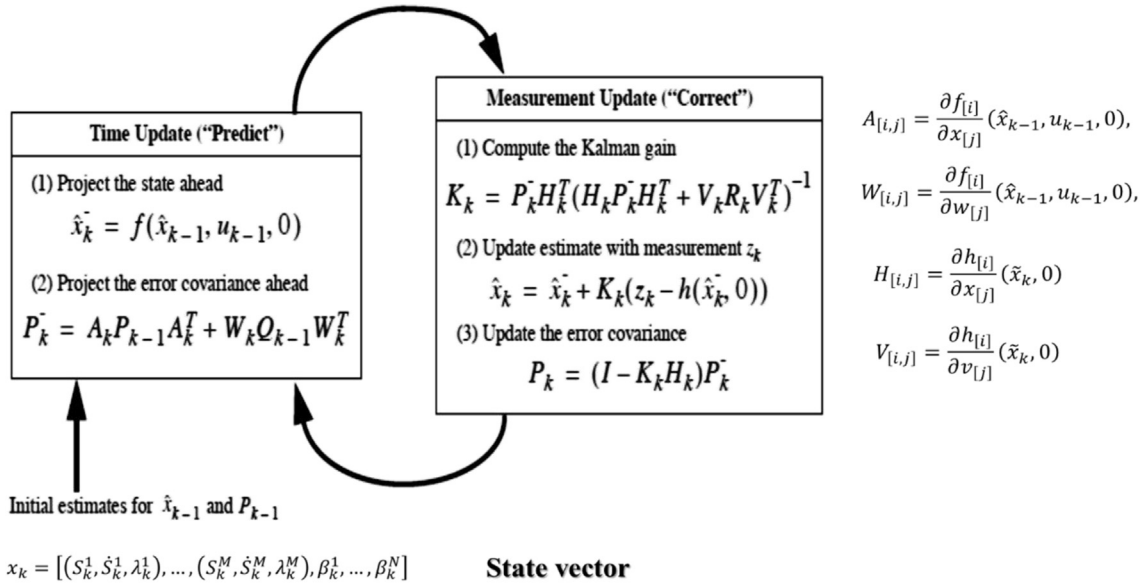

Fig. 1. A schematic view of EKF as the core of ENIF (Up) as well as the state vector engaged in imaging problem (Down) [16].

$$\boldsymbol{R}_k = \begin{bmatrix} \sigma^2 \Sigma_k^{\mathrm{GPS}} & 0 & 0 \\ 0 & \gamma^2 \mathbf{I} & 0 \\ 0 & 0 & \rho^2 \mathbf{I} \end{bmatrix} \tag{5}$$

In this matrix, Σ_k^{GPS} represents covariance matrix of GPS array, and $\mathbf{I}$ is the identity matrix. The constants in this matrix, (σ,γ,ρ), are known as the hyperparameters of the filter. Indeed, filter adjustment is done by changing these parameters along with some parameters in process model, (α, τ), which will be described in the following paragraphs. For example, γ and α controls the extent of spatial and temporal smoothing of slip rate distribution applied to the results, or σ controls the weight of fitness to the observed GPS data.

In the case of process model, state transition equation which predicts the state of the system at time k given an estimate of the state at time k-1, is linear and described as

$$\widehat{x}_k^- = A\widehat{x}_{k-1} + \delta_k, \qquad \delta_k \sim N(0, Q_k) \tag{6}$$

$$\boldsymbol{A} = \begin{bmatrix} \begin{pmatrix} 1 & \Delta t & 0 \\ 0 & 1 & 0 \\ 0 & 0 & 1 \end{pmatrix} & 0 & 0 \\ 0 & \ddots & 0 \\ 0 & 0 & \mathbf{I} \end{bmatrix}$$

$$\boldsymbol{Q} = \begin{bmatrix} \begin{pmatrix} \frac{\alpha^2}{3}\Delta t^3 & \frac{\alpha^2}{2}\Delta t^2 & 0 \\ \frac{\alpha^2}{2}\Delta t^2 & \alpha^2 \Delta t & 0 \\ 0 & 0 & \alpha^2 \frac{4}{5}\sqrt{\Delta t} \end{pmatrix} & 0 & 0 \\ 0 & \ddots & 0 \\ 0 & 0 & (\tau^2 \Delta t)\mathbf{I} \end{bmatrix}$$

where A, Q_k and δ_k indicate state transition matrix, process noise covariance matrix and process noise respectively. It should be mentioned that local benchmark motion at each station as well as slip rate of each subfault have been modeled as random walk motion with τ and α as their hyperparameters in this expression. Meanwhile, cumulative slip is modeled as integrated random walk. Application of such a model is common in tracking problems in which we have no knowledge about spatiotemporal evolution of our quantities of interest. Indeed, this is the very model allowing the filter to serve as a non-parametric estimation method which is a great advantage for the ENIF.

The key step prior to running the filter is the estimation of hyperparameters of the filter. According to the McGuire and Segall [9], the hyperparameters of the filter are calculated using maximum-likelihood estimation method which is based on the decomposition of prediction errors $(z_k - h(\widehat{x}_k^-, 0))$, or residuals, in the correction step of the filter. The goal of this method of estimation is to find a set of hyperparameters for which the occurrence likelihood of the observed data is maximal in the filtering phase of the algorithm. Such an optimization problem is innately nonlinear and requires application of global search methods. Accordingly, in this study, GA (Genetic Algorithm) were used to find the optimal values of hyperparameters of the filter. It should be highlighted that the only measurement model and its corresponding data involved in the likelihood calculation are GPS observations, z_k^{GPS}, and its measurement model (eq. (2)), thus the pseudo-data will have no contribution in the maximum likelihood estimation of hyperparameters.

Among all the relations involved in measurement model, eq. (3) is responsible for applying spatial smoothing constraint to the slip rate solutions. This constraint is imposed using Laplacian operator. In fact, this is the constraint causing over-smoothing phenomenon. To mitigate disruptive effect of this constraint, one idea is that if we could somehow detect slipping portion of the fault, instead of globally smoothing we can enforce spatial smoothing onto the slipping portion. To do so, we have incorporated an image segmentation step in the ENIF to detect the slipping portion at first place and then, based on the segmented image the process and measurement models are modified to enforce the algorithm to exert spatial smoothing only inside the slipping portion. In this study, Otsu method of segmentations along with some mathematical morphology analysis techniques (Erosion and Dilation) have been used for image segmentation

[17,18]. Because at the initial steps of processing, displacement signal from slow slip event compared to the background noise is too weak, the imaging problem is critical in these steps and we are temporarily facing with a very low SNR (signal to noise ratio) problem. As a result, we give the standard ENIF enough time until slow slip signal in the data gets stronger and concurrently slipping portion of the fault becomes more distinct in the images. Afterwards, the segmentation step and model modifications are applied to the standard ENIF. Visual inspection of slip images reveals that at step $k = 44$, or $t = 0.22$, the slipping portion of the fault emerges from the background image noise and correspondingly the deformation signal is also distinctive from the noise in the time series, so we start the segmentation process at this step and continue it up to the end of time series.

In the Otsu method of segmentation, we assume that our image of interest constitutes of two classes of pixels, e.g. foreground and background. In other words, histogram of its pixel intensities has a bimodal shape. In this situation, the goal is to find a threshold intensity for which the joint scattering of the classes (intra-class variances) is minimal. It has been proved that minimization of intra-class variance is equivalent to maximizing inter-class variance [17]. On the importance of segmentation step, it's suffice to say that choosing the threshold intensity has a profound effect on the performance of the algorithm. The higher the threshold intensity is, the smaller the foreground segment (slipping segment in our case) will be. In this situation, the algorithm is prone to completely eliminate the slipping portion of the fault during erosion stage. As a consequence, the stability of the algorithm highly depends on the appropriate selection of starting step for segmentation and we must be sure that the slipping portion of the image will not be lost during erosion step. For example, in the cases like Cascadia which shows small events, the algorithm is likely to completely eliminate the slipping segment and consider the whole fault as a silent region which leads to an instable filtering process. On the other hand, in the Mexico which contains larger events, it is less possible for the instability to occur. In one word, it is up to the user to control the stability of the algorithm by choosing the starting segmentation step and monitoring the slipping portions during the filtering procedure.

To describe segmentation process more clearly, Fig. 2 depicts this process at time step $k = 44$, where the segmentation process begins.

As is clear in Fig. 2, dilation operation of mathematical morphology is performed in two successive steps. This results in a slipping portion which is somewhat larger than actual size. Consequently, a larger region makes the algorithm capable of imaging slow slip events which grow with time. Also, as the algorithms proceeds with time, the segmented active zone (slipping region) converges to the true slipping region.

It is worth noting that image segmentation is merely performed to modify the process and measurement models involved in the ENIF formulation and it has nothing to do with the uncertainty propagation. The uncertainty propagation is performed as before so that in the ENIF with EKF (Extended Kalman Filter) uncertainty propagation is done by linearization of non-linear models through calculation of Jacobian and Hessian matrices. In the case of ENIF with UKF (Unscented Kalman Filter) this uncertainty propagation is performed using UT (Unscented Transform) which will be explained in more details at the end of this section. Therefore, once slipping portion of the fault is detected in segmentation step, some changes in the process and measurement models are made as follows. A new constraint which tries to assign zero slip value to subfaults in non-slipping region (silent zone) is included in measurement model.

$$z_k^{\text{zero}} = 0 = S_k^i + \epsilon_k, \qquad i \in \{\text{silent zone}\} \qquad \epsilon_k \sim N\left(0, \eta^2 \mathbf{I}\right) \tag{7}$$

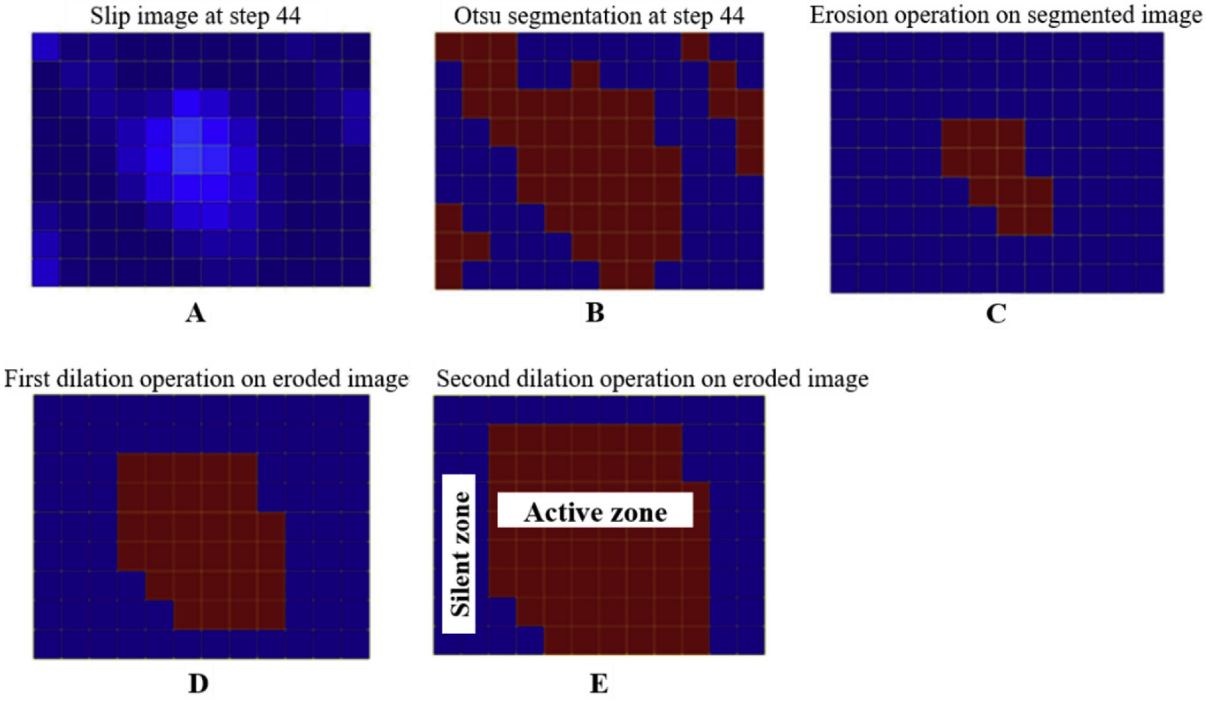

Fig. 2. Segmentation procedure at 44th time step. **A)** Slip image resulted from measurement update at this time step. **B)** Otsu segmentation of slip image. **C)** Eroding the segmented image. **D)** Dilation operation on eroded image at step C. **E)** Performing an extra dilation operation on the eroded image.

At the same time, the pseudo-data corresponding to this constraint (z_k^{zero}) should be included in the data vector resulting in a new augmented data vector in the form of $z_k = [z_k^{\text{GPS}}, z_k^{\nabla}, z_k^{+}, z_k^{\text{zero}}]$. With the definition of this new constraint, a new hyperparameter η, is introduced here. Since we intend to highly enforce the algorithm to zero the slip for subfaults inside the silent zone, the value assigned to this hyperparameter is considered to be small. Similarly, some changes in the process model is required too. Actually, by these changes we consider two different process models for each portion of the fault. The process model for slipping portion (active zone) is the same as the standard ENIF, but in the case of non-slipping region, or silent zone, the process model makes slip rata and slip independent of each other. In this way, the slip rate in the silent zone is made to be zero, while the slip remains unchanged. Later on, non-zero slip values in the silent zone are forced to be zero through measurement model (Eq. (7)). Therefore, the new process model is

$$\widehat{x}_k^- = A'\widehat{x}_{k-1} + \delta_k', \qquad \delta_k' \sim N\left(0, Q_k'\right) \tag{8}$$

$$\boldsymbol{A}' = \begin{pmatrix} A_j & 0 & 0 \\ 0 & \ddots & 0 \\ 0 & 0 & \mathbf{I} \end{pmatrix}$$

$$\boldsymbol{A}_j = \begin{cases} \begin{pmatrix} 1 & \Delta t & 0 \\ 0 & 1 & 0 \\ 0 & 0 & 1 \end{pmatrix} & \text{if} \quad j\epsilon\{\text{Active slip one}\} \\ \begin{pmatrix} 1 & 0 & 0 \\ 0 & 0 & 0 \\ 0 & 0 & 1 \end{pmatrix} & \text{if} \quad j\epsilon\{\text{Inactive slip zone}\} \end{cases}$$

$$Q' = \begin{pmatrix} B_j & 0 & 0 \\ 0 & \ddots & 0 \\ 0 & 0 & (\tau^2\Delta t)\mathbf{I} \end{pmatrix} \qquad B_j = \begin{cases} \begin{pmatrix} \frac{1.5\alpha^2}{3}\Delta t^3 & \frac{1.5\alpha^2}{2}\Delta t^2 & 0 \\ \frac{1.5\alpha^2}{2}\Delta t^2 & 1.5\alpha^2\Delta t & 0 \\ 0 & 0 & 1.5\alpha^2\frac{4}{5}\sqrt{\Delta t} \end{pmatrix} & \text{if j}\epsilon\{\text{Active slip one}\} \\ \begin{pmatrix} \frac{\mu}{3}\Delta t^3 & 0 & 0 \\ 0 & \mu\Delta t & 0 \\ 0 & 0 & \mu\frac{4}{5}\sqrt{\Delta t} \end{pmatrix} & \text{if j}\epsilon\{\text{Inactive slip zone}\} \end{cases}$$

Again, along the introduction of the new process model for silent zone of the fault, a new hyperparameter μ, emerges in the covariance matrix of process noise model Q'. Like before, the value of this hyperparameter is set to be small. Such a process model with small hyperparameters at the covariance matrix will have a pivotal role in the smoothing stage of the algorithm, when the remaining cumulative slip in the silent zone of the fault will be removed with a backward smoothing. At the same time, to capture any abrupt increase caused by migration of slip into the active zone, the covariance matrix of subfaults inside the active zone is widened by a factor of 1.5.

As was mentioned earlier, due to nonlinearity imposed by non-negativity constraint of slip rate, uncertainty propagation through measurement model is a challenging part of imaging problem and we proposed application of UKF as an alternative for EKF. Accordingly, as an alternative to EKF, we have also investigated the application of UKF for imaging problems. UKF uses UT for uncertainty propagation. According to Ref. [14], the basic idea behinds UT is "With a fixed number of parameters it should be easier to approximate a given distribution than it is to approximate an arbitrary nonlinear function/transformation." Having this notion in mind, Fig. 3 gives us a comparative example of mean and covariance propagation through different methods applied in this study.

Here, we provide a brief description on how UT is performed in general. Given a normal distribution with mean $\bar{x}$ and covariance Σ_x, a set of $p+1$ sigma points with associated weights, $\mathscr{S} = \{i = 0, 1, \ldots, p : x^{(i)}, W^{(i)}\}$, are chosen so that satisfy the following relations:

$$\sum_{i=0}^{p} W^{(i)} = 1 \tag{9}$$

$$\bar{x} = \sum_{i=0}^{p} W^{(i)} x^{(i)} \tag{10}$$

$$\Sigma_x = \sum_{i=0}^{p} W^{(i)} \left\{x^{(i)} - \bar{x}\right\}\left\{x^{(i)} - \bar{x}\right\}^{\mathrm{T}} \tag{11}$$

It is worth noting that the weights $W^{(i)}$, could have positive or negative values. Having these sigma points mapped through a nonlinear function $h(x)$, we obtain nonlinearly transformed sigma points $z^{(i)}$, with mean $\bar{z}$, and covariance Σ_z, as follows:

$$z^{(i)} = h\left[x^{(i)}\right] \tag{12}$$

$$\bar{z} = \sum_{i=0}^{p} W^{(i)} z^{(i)} \tag{13}$$

$$\Sigma_z = \sum_{i=0}^{p} W^{(i)} \left\{z^{(i)} - \bar{z}\right\}\left\{z^{(i)} - \bar{z}\right\}^{\mathrm{T}} \tag{14}$$

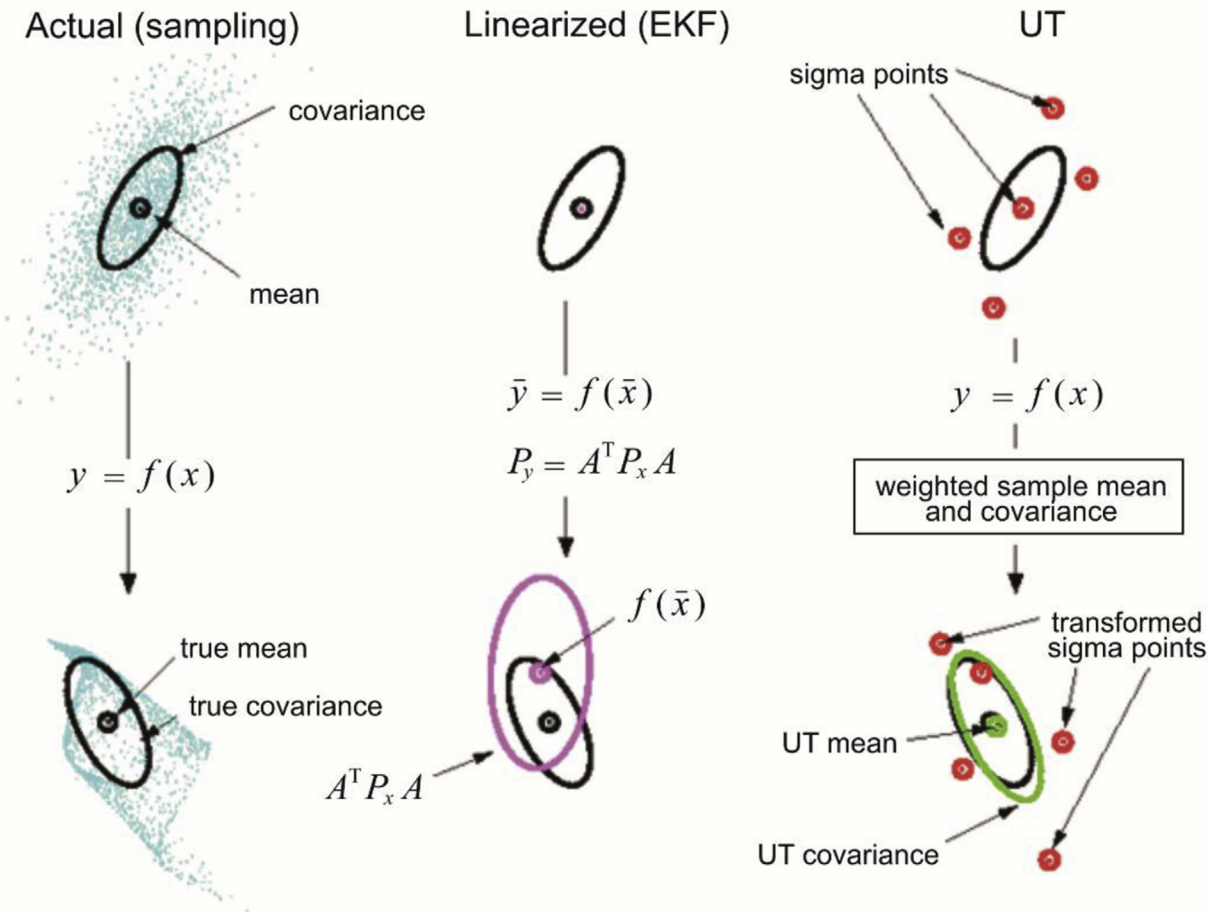

Fig. 3. A comparison on different uncertainty propagation. **Left:** actual propagation with a bunch of random points. **Middle:** propagation by linearization of non-linear function. **Right:** propagation by sigma points [19].

Actually, the provided equations explain how the uncertainty is propagated through any non-linear model and we can recover the mean and covariance matrix of a distribution after a non-linear mapping by UT method. In our study, such an uncertainty propagation technique is applied in the correction step of UKF where we need to propagate predicted state $\widehat{x}_k^-$, and its associated uncertainty P_k^-, through measurement model.

Finally, since Kalman filter is a forward filter in time, at each time step, state vector is estimated given the date up to that time step. In order to estimate state vector given all the data, previous and subsequent data, the same procedure is performed backward in time using Kalman smoothing. This algorithm is also known as RTS (Rauch-Tung-Striebel smoother) and has been developed by [20–22]. The goal of the RTS smoother is to compute the smoothing solution for the state vector of interest given as distribution

$$p(x_k|y_{1:T}) = N(x_k|\widehat{x}_k^s, P_k^s) \tag{15}$$

This equation states that the final solution will have a normal distribution with a mean equal to smoothed solution $\widehat{x}_k^s$, and its associated covariance matrix P_k^s. This mean and covariance are calculated backward in time according the following procedure.

$$\widehat{x}_k^- = A\widehat{x}_{k-1} \tag{16}$$

$$P_k^- = AP_{k-1}A^{\mathrm{T}} + Q_k \tag{17}$$

$$C_{k-1} = P_{k-1}A^{\mathrm{T}}\left[P_k^-\right]^{-1} \tag{18}$$

$$\widehat{x}_{k-1}^s = \widehat{x}_{k-1} + C_{k-1}\left[\widehat{x}_k^s - \widehat{x}_k^-\right] \tag{19}$$

$$P_{k-1}^s = P_{k-1} + C_{k-1}\left[P_k^s - P_k^-\right]\ C_{k-1}^{\mathrm{T}} \tag{20}$$

where $\widehat{x}_{k-1}^s$ and P_{k-1}^s represent the smoother estimates for the mean and covariance of state vector in time step k-1, while $\widehat{x}_{k-1}$ and P_{k-1} represent the filter estimates for the state mean and covariance on the time step k-1 and finally, $\widehat{x}_k^-$ and P_k^- are the predicted mean and covariance at time step k which are the same as in Kalman filter and C_{k-1} is the counterpart of Kalman gain in the smoothing procedure on time k-1 and is known as smoothing gain. As is clear from this formulation, the only model used in the smoothing procedure is process model. Accordingly, in this study, the process model used for smoothing purpose is the modified model after segmentation at the last time step (Eq. (8)). Besides the smoothing of slip and slip rate history inside the active zone, this model will remove the slip remained up to the time step at which the subfault has been recognized to belong with a silent zone (Fig. 5).

3. Results and discussion

To test the performance of our proposed algorithm, we have implemented it to a low signal to noise ratio synthetic data set. For this purpose, we considered a hidden 240 km long, 90 km wide and 20° dip strike-slip fault in a half-space medium with a hidden depth of 10 km. To assign a slow slip event to the fault, the fault were divided into 108 subfaults with a length and width of 20 km and 10 km respectively. Then, using a rectangular array constituting of 64 of GPS stations deployed on the Earth's surface (Fig. 4), noise contaminated slow slip signal resulting from an imaginary slow slip event on the fault is recorded. The event is a combination of three radial patches, each of which has an S shape slip history starting with zero and ending up with the maximum slips of 40, 32 and 24 mm respectively for inner, middle and outer patches during a time span of 0.5 year. In this regard, disloc3d, a Matlab wrapper to Y. Okada's DC3, is used as forward model [23]. Finally, the deformation signal of the event is contaminated with two kind of noises: a white noise with the parameter of $\sigma = 0.5$ mm and colored noise random benchmark motion with the parameter of $\tau = 0.7$ mm/year$^{\frac{1}{2}}$.

The same hyperparameters used for standard ENIF are applied for our proposed algorithm with this exception that the assigned values for η, ρ and μ, are considered to be very small, meaning that we highly accentuate their corresponding constraints and process noise covariance. These set of small hyperparameters are identical for both filter cores and their values are: $\eta = 1$ mm, $\rho = 10^{-12}$ and $\mu = 10^{-5}$. Table 1 shows the values of the other hyperparameters obtained from maximum likelihood estimation for both standard ENIF with EKF and UKF as core.

Fig. 5 illustrates derived images from different methods besides the true slow slip event used for generation of synthetic data.

As is shown in Fig. 5, segmentation based ENIF has the potential to remove clutters surrounding slipping region in recovered images. The existence of these clutters could be explained by another limitation of standard ENIF. As was noted earlier, at the initial steps of imaging problem the noise is dominant in the date and the algorithm is prone to model noise in the form of clutters. But because of the non-negativity constraint of slip rate, the algorithm is not able to remove the clutters and they remain on the images.

Table 1
Maximum likelihood estimation of hyperparameters of the standard ENIF with different cores.

Filter core type	$\widehat{\alpha}$	$\widehat{\gamma}$	$\widehat{\sigma}$	$\widehat{\tau}$
EKF	387	491	0.45 mm	0.78 mm/yr$^{\frac{1}{2}}$
UKF	285	293	0.59 mm	0.61 mm/yr$^{\frac{1}{2}}$

In addition, Fig. 6 illustrates the slip history of some subfaults located at respectively silent zone, the edge of active zone and the center of active zone with a maximal amount of cumulative slip. As is shown in Fig. 6, at somewhere around $t = 0.35$, the algorithm has recognized that the subfault with the indices of $i = 8$ and $j = 7$ belongs to the silent zone and then its slip is set to the zero until the end of the time series is reached. Later, the remaining slip prior to this time will be removed during the backward smoothing procedure. The impact of this zeroing on the adjacent subfaults and all the elements inside the active zone could be a slight increase in their slip values. Every time a subfault is set to zero, its cumulative slip is expected to be distributed among active region. Another remarkable phenomenon in this figure is the existence of some temporary drops in the slip which means that at some times the non-negativity constraint could not strictly guarantee for the slip rate to be non-negative. In our view, most of instabilities of the ENIF stems from this constraint and it should somehow be modified at future version.

We need a mathematical measure to quantitatively evaluate the performance of our proposed algorithm and compare the results from different methods. Accordingly, following McGuire and Segall [9], the summed squared residual between the true slip and slip rate and their estimated counterparts used in this study is as follows:

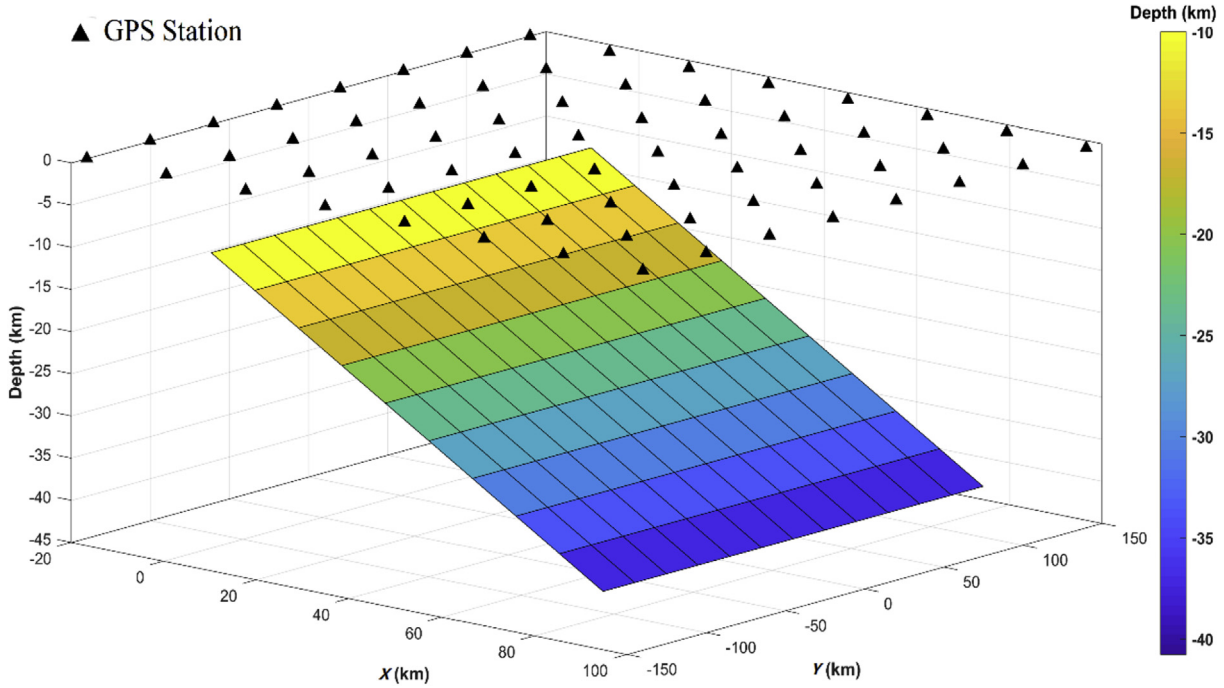

Fig. 4. A view of the fault geometry and location of GPS stations on the surface. Black triangles represent the GPS stations.

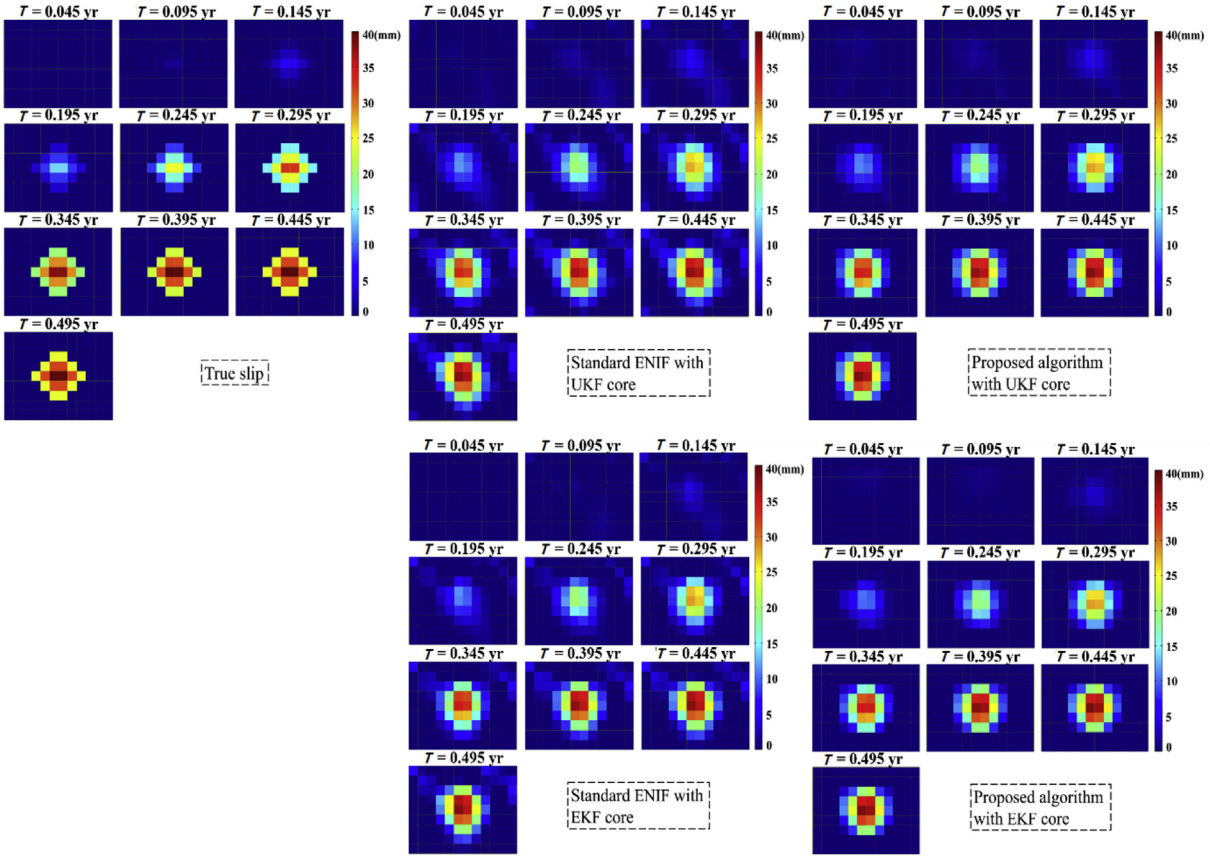

Fig. 5. True slip versus recovered slip images by different algorithms.

$$R_{sr} = \frac{\sum_k \sum_i \sum_j \left(\dot{S}_{i,j}^k - \hat{\dot{S}}_{i,j}^k \right)^2}{\dot{S}_{i,j}^k}$$
$$R_s = \frac{\sum_k \sum_i \sum_j \left(S_{i,j}^k - \hat{S}_{i,j}^k \right)^2}{S_{i,j}^k} \quad (21)$$

where $\dot{S}$ and S respectively represent slip rate and slip. Hatted symbols represent estimated quantities by the algorithm, whereas hat free symbols are their true counterparts. In addition, i and j indicate the subfault indices and k represents the time step. Table 2 shows these measures for each algorithm.

These results show a considerable improvement when segmentation step is incorporated into standard ENIF in the both cases of UKF and EKF as core. However, despite our expectation that UKF would outperform EKF, the results show that the EKF still has the better results. This issue could have roots in measurement model where except non-negativity, all the constraint are linear. This indicates that ENIF system models tend to be linear and in this situation linearization could be a reasonable approximation.

Another promising result about segmentation method is revealed when each time series is decomposed to its constituent signals. Decomposition of data in many GPS stations proved that segmentations is quite helpful in distinguishing between different signals. Fig. 7, for example, shows the data decomposition in one of the stations with interesting results. While standard ENIF with UKF core has mistaken local benchmark motion for slow slip signal, our proposed algorithm with UKF core is successful in tracking these signals.

4. Conclusions

Our proposed algorithm with incorporation of an image segmentation step into ENIF proved to be effective in terms of the summed squared residual. By removing clutters in the images and enforcing the smoothing constraint onto the slipping portion of the fault, this method is quite successful in isolating the slow-slip signal from background noise. However, application of UKF as replacement for EKF in the ENIF's core didn't necessarily yield better results. To apply this algorithm in real world applications, we need to consider some relevant limitations that its resolution forms the subject of our future works. First, although this algorithm performs very well in the case of single slipping events, it is prone to some instabilities for some more sophisticated events like the existence of multiple slipping regions. For example, during an initial slip event another slow slip event nucleate somewhere else on the fault, this algorithms will not be able to model this subsequent event. Another limitation of this method is concerned with the occurrence of a coseismic event, which has a sharp slip and slip rate changes compared with interseismic events, during the time span of our study. Such an event would also impose an instability to the algorithm and leads to a wrong answers. In terms of inverse problems, due to the nature of measurement model, we are dealing with a non-linear inverse problems. Typically, these problems are solved using iterative methods, like Newtonian-based approaches, in

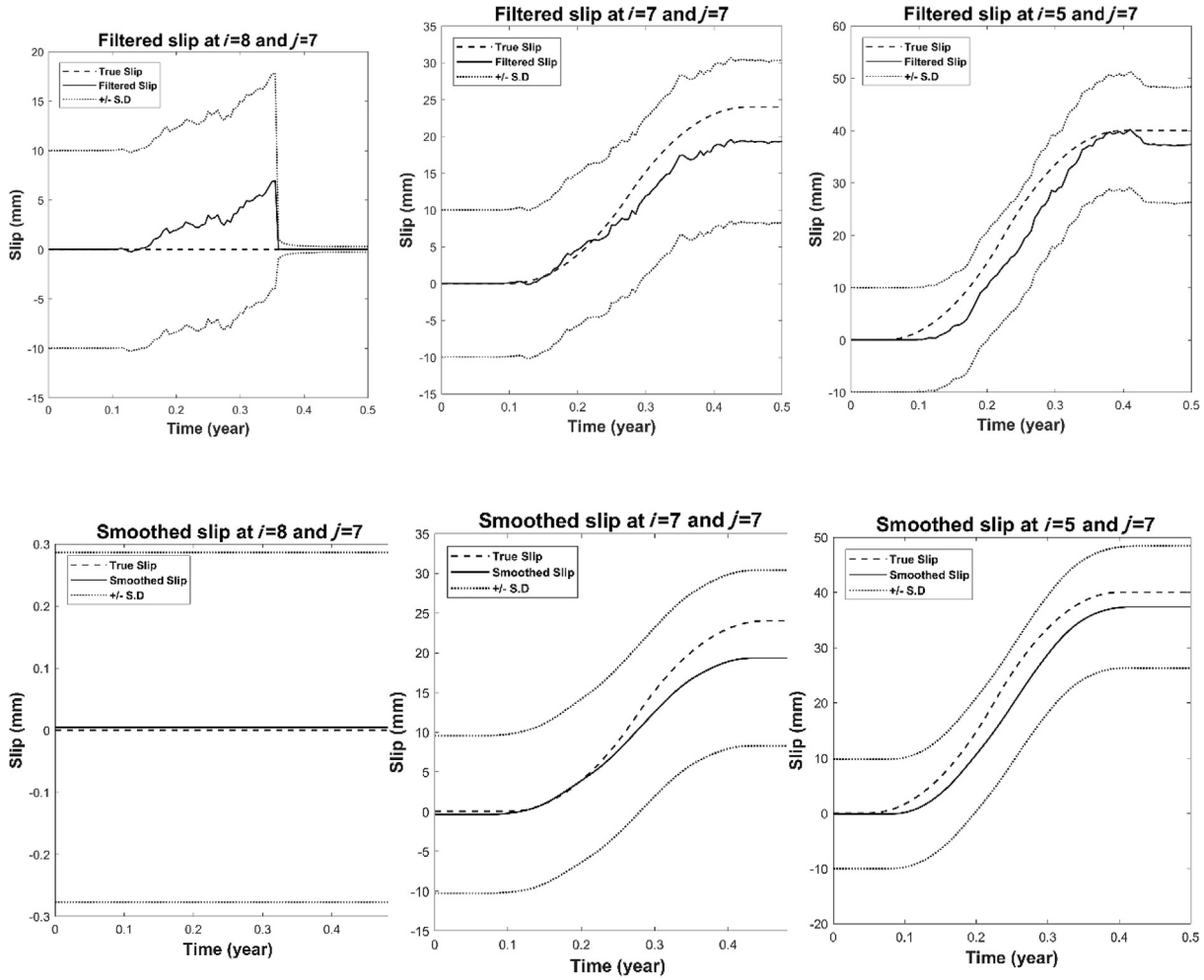

Fig. 6. Slip history of some subfaults located at respectively silent zone (left), edge of active zone (middle) and a subfault at the region with maximal cumulative slip (right), after filtering (up) and smoothing (down) procedure obtained by proposed algorithm with EKF as core. *i* and *j* indicate the indices of the subfault on the rectangular fault.

Table 2
Performance of different algorithms in terms of measures introduced in Eq. (21).

Measure	Standard ENIF with UKF core	Standard ENIF with EKF core	Proposed algorithm with UKF core	Proposed algorithm with EKF core
R_s	0.182	0.126	0.089	0.079
R_{sr}	0.285	0.215	0.147	0.129

which we start with an initial solution and using Taylor expansion of the model, the initial solution is updated to converge toward the true solution. However, in the EKF and UKF framework, this procedure is performed only by one iteration (correction step in Fig. 1). In the case of interseismic events, with a sufficiently accurate guess for the state vector at $t = 0$, due to the nature of such events, the solution for successive time steps are expected to be in close proximity of each other and thus we can hope a single iteration would suffices for the algorithm to yield a reasonably accurate solution. In the case of coseismic events, however, the situation is not so simple. If we consider the predicted state, $\widehat{x}_k^-$, as an initial solution for the inverse problem, this solution is far from the true solution and as a consequence, we cannot reach the true solution by only one iteration. The reason for such a large distance in the solution space is the fact that the predicted state is obtained from an interseismic process model through which slip and slip rate changes very slowly, while in the reality a coseismic event with a sharp rise in slip and slip rate has been occurred. To tackle with this limitation, one suggestion could be solving the coseismic imaging problem outside of the algorithm using such a diverse set of data as seismic, geodetic, etc., and then incorporating the results into the algorithm using some modifications of measurement model at the time steps coincident with coseismic event. Besides some other modifications, in our future studies we are going to take this situation into account and develop a more rigorous algorithm. Some of these modifications are as follows. Firstly, we are going to develop an adaptive version of ENIF which changes its hyperparameters with time so as to accommodate itself to changes in slip rates at different phases of slow slip event. Moreover, developing a robust version of this algorithm, which is able to detect outlier time series and mitigate their destructive effect, would results in an automatic method for online monitoring of slow slip events. Finally, since triangular subfault models have better fitness to the fault plane geometry, specifically to curved subduction zones, we are considering the use of new measurement models which are based on triangular subfault models. After introducing these modifications, the resulting algorithm have the potential to be applied for real-time applications.

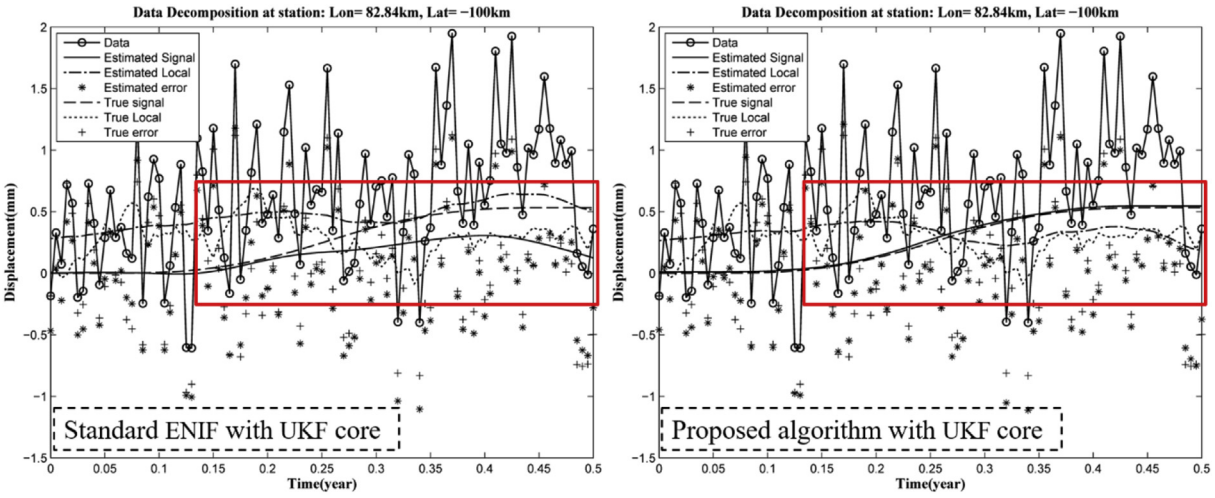

Fig. 7. Data decomposition of GPS time series into constituent true signals and estimated by different algorithms. **Left:** Standard ENIF with UKF core is wrong in tracking different signals. **Right:** Proposed algorithm with UKF core successfully distinguish true deformation signal caused by slow-slip event from local benchmark motion.

Acknowledgements

We would like to show our gratitude to the International Association of Geodesy (IAG) and Secretary General Herman Drewes, for providing us with financial support to present the current study in this symposium. We are also immensely grateful to Carla Braitenberg for her generous support in the symposium.

References

[1] J.R. Leeman, D.M. Saffer, M.M. Scuderi, C. Marone, Laboratory observations of slow earthquakes and the spectrum of tectonic fault slip modes, Nat. Commun. 7 (2016).
[2] A.T. Linde, P.G. Silver, Elevation changes and the great 1960 Chilean earthquake: support for aseismic slip, Geophys. Res. Lett. 16 (11) (1989) 1305–1308.
[3] A. Kato, K. Obara, T. Igarashi, H. Tsuruoka, S. Nakagawa, N. Hirata, Propagation of slow slip leading up to the 2011 Mw 9.0 Tohoku-Oki earthquake, Science 335 (6069) (2012) 705–708.
[4] R. Bilham, N. Ambraseys, Apparent Himalayan slip deficit from the summation of seismic moments for Himalayan earthquakes, 1500–2000, Curr. Sci. 88 (10) (2005) 1658–1663.
[5] P. Segall, E.K. Desmarais, D. Shelly, A. Miklius, P. Cervelli, Earthquakes triggered by silent slip events on Kīlauea volcano, Hawaii, Nature 442 (7098) (2006) 71–74.
[6] D. Zigone, D. Rivet, M. Radiguet, M. Campillo, C. Voisin, N. Cotte, A. Walpersdorf, N.M. Shapiro, G. Cougoulat, P. Roux, V. Kostoglodov, Triggering of tremors and slow slip event in Guerrero, Mexico, by the 2010 Mw 8.8 Maule, Chile, earthquake, J. Geophys. Res. Solid Earth 117 (B9) (2012).
[7] A. Santamaría-Gómez, M.N. Bouin, X. Collilieux, G. Woeppelmann, Correlated errors in GPS position time series: implications for velocity estimates, J. Geophys. Res. Solid Earth 116 (B1) (2011).
[8] P. Segall, M. Matthews, Time dependent inversion of geodetic data, J. Geophys. Res. 102 (1997) 22–391.
[9] J.J. McGuire, P. Segall, Imaging of aseismic fault slip transients recorded by dense geodetic networks, Geophys. J. Int. 155 (3) (2003) 778–788.
[10] D.P.S. Bekaert, P. Segall, T.J. Wright, A.J. Hooper, A Network Inversion Filter combining GNSS and InSAR for tectonic slip modeling, J. Geophys. Res. Solid Earth 121 (2016) 2069–2086.
[11] H.B. Mitchell, Multi-sensor Data Fusion: An Introduction, Springer Science & Business Media, 2007.
[12] B.W. Reutter, G.T. Gullberg, R.H. Huesman, Direct least-squares estimation of spatiotemporal distributions from dynamic SPECT projections using a spatial segmentation and temporal B-splines, IEEE Trans. Med. Imag. 19 (5) (2000) 434–450.
[13] J. Qranfal, Incorporating nonnegativity and spatial regularization constraints using proximal projections, Int. J. Pure Appl. Math. 81 (2) (2012) 267–304.
[14] S.J. Julier, J.K. Uhlmann, Unscented filtering and nonlinear estimation, Proceedings of the IEEE 92 (3) (2004) 401–422.
[15] J. Hartikainen, A. Solin, S. Särkkä, Optimal Filtering with Kalman Filters and Smoothers, Department of Biomedica Engineering and Computational Sciences, Aalto University School of Science, Greater Helsinki, Finland, 2011, 16.
[16] G. Welch, G. Bishop, An Introduction to the Kalman Filter, Department of Computer Science, University of North Carolina, 2006.
[17] Nobuyuki Otsu, A threshold selection method from gray-level histograms, IEEE Transactions on Systems, Man, and Cybernetics 9 (1) (1979) 62–66.
[18] E.R. Dougherty, An Introduction to Morphological Image Processing, Tutorial texts in optical engineering, 1992.
[19] A. UmaMageswari, J.J. Ignatious, R. Vinodha, A comparitive study of Kalman filter, extended kalman filter and unscented Kalman filter for harmonic analysis of the non-stationary signals, Int. J. Sci. Eng. Res. 3 (7) (2012) 1–9.
[20] H.E. Rauch, C.T. Striebel, F. Tung, Maximum likelihood estimates of linear dynamic systems, AIAA J. 3 (8) (1965) 1445–1450.
[21] A. Gelb (Ed.), Applied Optimal Estimation, MIT press, 1974.
[22] Y. Bar-Shalom, X.R. Li, T. Kirubarajan, Estimation with Applications to Tracking and Navigation: Theory Algorithms and Software, John Wiley & Sons, 2004.
[23] Y. Okada, Internal deformation due to shear and tensile faults in a half-space, Bull. Seismol. Soc. Am. 82 (2) (1992) 1018–1040.



Mohammad Hazrati Kashi (SM'99) was born in Kashan, Iran, in 1985. He received the B.E. degree in Mining engineering from the University of Tehran, Tehran, Iran, in 2010, and the M.Sc. degree in Geophysics with a major in Earthquake Seismology from the Institute of Geophysics, University of Tehran, Tehran, Iran, in 2013. In 2014, he joined the Research Center for Earthquake Precursors, University of Tehran, to spend his 2 year period of military services as a researcher. Since 2016, he has been working in Keymand Energy Pars Company (KEPCO), a pioneer company in applying advanced technology for Quality Control (QC) purposes in Iran. He is also an active member of a Non-Governmental Organization (NGO) working on awareness campaigns against health issues like infertility and cervical cancer. His main areas of research interest are Theoretical Inverse Problems in Geophysics with an especial focus on joint inversion of geodetic data. He is also interested in applying uncertainty quantification techniques for stochastic estimation of geophysical phenomena.